

Nanoconfined Expansion Behavior of Hollow MnS@Carbon Anode with Extended Lithiation Cyclic Stability

Zhipeng Ma, Ailing Song, Zhan Liu, Yaqian Guo, Xin Yang, Qing Li, Yuqian Fan, Lei Dai,* Hao Tian,* Xiujuan Qin, Hao Liu,* Guangjie Shao,* and Guoxiu Wang*

The construction of hollow nanostructure by compositing with carbonaceous materials is generally considered an effective strategy to mitigate the drastic volume expansion of transition metal sulfides (TMSs) with high theoretical specific capacity in the process of lithium storage. However, designing well-controlled architectures with extended lithiation cyclic stability, and ease the expansion of the electroactive materials into the reserved hollow spaces still needs to be developed. Herein, using MnS as an example, the hollow double-shell carbon-coated TMSs architecture is designed to achieve the controllable operation of shell thickness to regulate interfacial stress. The functional architecture enables the high-capacity MnS to reach reversible capacities and extended lithiation cycling stability at high current densities. In situ transmission electron microscopy, optical observation characterizations and finite elements are used to analyze the nanoconfined expansion behavior of hollow MnS@C anodes. The as-designed hollow structure with a carbon shell thickness ≈ 12.5 nm can effectively restrict the drastic expansion of MnS nanoshell into inner voids with compressive stress. This study demonstrates a general strategy to design functional carbon coating metal sulfides with tailored interfacial stress.

and cycling life of LIBs. Transition metal sulfides (TMSs) based on a conversion-type lithium storage mechanism, including manganese sulfide (MnS), zinc sulfide (ZnS), and nickel sulfide (NiS_x), have been recognized as the most important candidates due to their high theoretical specific capacities, low-cost and environmental friendliness.^[2] Nevertheless, TMSs-based electrode materials with high capacities are generally accompanied by a large volume expansion in the process of lithiation, which results in severe structural collapse and progressive electrode pulverization. Furthermore, combined with the inherent features of poor electronic/ionic conductivity of TMSs, the actual capacity and cyclic stability are far from meeting desirable requirements, thus limiting their practical applications.^[2a,b]

Considerable efforts, such as nanostructure engineering and heterostructure construction, have been devoted to enhancing cycling stability and performance of TMSs as anode materials in LIBs.^[2a,3] Among them, the hollow nanostructure engineering of the carbon layer-coated TMSs is customized to improve electron transfer, shorten the ion diffusion path, and accommodate the volume change during cycling.^[2b-f,4] The conductive carbon shell can not only enhance the electronic conductivity of electroactive materials but also inhibit the agglomeration of electroactive materials

1. Introduction

Rechargeable lithium-ion batteries (LIBs) have been considered as the most promising electrochemical energy storage supply systems for portable electronics and electric vehicles.^[1] The development of high-capacity and ultra-stable electrode materials is the key issue for improving the energy density

Z. Ma, A. Song, Z. Liu, Y. Guo, X. Yang, Q. Li, Y. Fan, X. Qin, G. Shao
Hebei Key Laboratory of Applied Chemistry
Hebei Key Laboratory of Heavy Metal Deep-Remediation in Water and Resource Reuse
College of Environmental and Chemical Engineering
Yanshan University
Qinhuangdao 066004, China
E-mail: shaoguangjie@ysu.edu.cn

© 2023 The Authors. Advanced Functional Materials published by Wiley-VCH GmbH. This is an open access article under the terms of the Creative Commons Attribution License, which permits use, distribution and reproduction in any medium, provided the original work is properly cited.

 The ORCID identification number(s) for the author(s) of this article can be found under <https://doi.org/10.1002/adfm.202301112>.

DOI: 10.1002/adfm.202301112

L. Dai
College of Chemical Engineering
North China University of Science and Technology
Tangshan 063009, China
E-mail: dailei@ncst.edu.cn

H. Tian, H. Liu, G. Wang
Centre for Clean Energy Technology
School of Mathematical and Physical Sciences
Faculty of Science
University of Technology Sydney
Broadway, Sydney, NSW 2007, Australia
E-mail: hao.tian@uts.edu.au; hao.liu@uts.edu.au;
guoxiu.wang@uts.edu.au

G. Shao
State Key Laboratory of Metastable Materials
Science and Technology
Yanshan University
Qinhuangdao 066004, China

during cycling processes, thereby leading to the enhancement of cycling stability and rate capability.^[4d–f,5] The inner voids of hollow structures can offer enough space to cushion the volume change during lithium storage. In particular, the full contact between the inter electroactive materials and the carbon shell also plays an important role in ensuring the rapid transport of ions/electrons, as well as modulating the strain intensification caused by lithiation.^[6] Despite the considerable achievements in artifications, refined hollow-structured TMSs confined within carbon nanoshells with tailored interfacial stresses to accommodate the expansion behavior during lithiation/delithiation processes in LIBs is still remained to be developed and studied.^[5d,f,h–j,7]

Herein, we developed a general synthetic strategy of confinement template evolution to design hollow double-shell carbon-coated TMSs (MS@C, M=Mn, Fe, and Sn) materials as high-capacity and stable anodes in LIBs. During the preparation, the inner core sulfur nanosphere was not only used as a self-template to tailor the inner diameter of the hollow structure but also used as sulfur source to vulcanize transition metals. The hollow structured MS@C with adjustable carbon shell thickness was achieved, controlling the interfacial stress during lithium continuous insertion. Subsequently, the interfacial stress between the carbon shell and the electroactive material MS effectively limited the expansion caused by lithium extension and accelerated the lithium-ion transport kinetics. Based on in situ characterization from nano- to macro-scale and finite element analysis, the optimized hollow MnS@C anode exhibited an impressive nanoconfined expansion behavior toward LIBs. When the thickness of carbon nanoshell was ~12.5 nm in hollow structures, the drastic expansion of MnS shell can be effectively restricted into inner voids with a compressive stress. The facile synthetic approach of utilizing sulfur nanospheres as a self-template is unique, reproducible, and adaptable, and the multi-scale research strategy can bring inspiration for the development of other high-performance anodes.

2. Results and Discussion

2.1. Formation Process and Characterization of Hollow Double-Shell MnS@C Structures

The volume expansion pattern of hollow double-shell MS@C nanospheres during the lithiation process depends on the distribution of interfacial stress between the electroactive materials and carbon. The detailed schematic structure transformation process is shown in **Figures 1a,b**. When the thickness of carbon coating layer is thinner, the interfacial stress between MS and carbon nanoshells tends to be from inside to outside in the process of lithiation, and the outward tensile stress prompts the expansion of MS to breach the restriction of the thin carbon nanoshell, finally leading to the collapse of the hollow structure (**Figure 1a**) and poor cycling stability of electrodes made therefrom. As the adjustable carbon coating layer thickens, the direction of interfacial stress gradually changes from an outward tensile stress to an inward compressive stress, which can ensure the expansion of MS into the reserved inner space, and accelerates the lithium-ion transport kinetics (**Figure 1b**).

The synthesis procedure for hollow double-shell MnS@C nanospheres, as a typical example, is illustrated in **Figure 1c**. Typically, the excess colloidal solution of sulfur nanospheres with a tailored diameter of ca. 700 ± 50 nm, was prepared according to our previous report as a self-template (**Figures S1 and S2**, Supporting Information).^[8] This is reacted with potassium permanganate solution in a 60 °C water bath to obtain S@MnO₂ core-shell nanospheres (**Figures S3–S6**, Supporting Information). In these, ultrathin δ -MnO₂ nanosheets are evenly grown on the surface of sulfur nanospheres to form a core-shell structure with a diameter of ca. 1 μ m. Then, a polydopamine layer with different thicknesses is coated on the surface of S@MnO₂ core-shell nanospheres by regulating the amount of dopamine monomer. These nanospheres are finally transformed into hollow double-shell MnS@C nanospheres with adjustable thickness of carbon coating layer after inert atmosphere heat treatment. Moreover, the synthesis strategy can be easily extended to prepare other hollow structures, such as iron-based sulfides@C (Fe_{1-x}S@C) and tin-based sulfides@C (SnS@C) hollow double-shell nanospheres (**Figures S7 and S8**, Supporting Information).

The crystalline phases of the three MnS@C samples were confirmed by X-ray diffraction (XRD) patterns (**Figure 1d**). It can be seen that all diffraction peaks are well assigned to stable α -MnS (JCPDS card No. 06–0518) without any detectable impurities, indicating the high phase purity. According to thermogravimetric analysis (TGA) (**Figure S9**, Supporting Information), the weight ratio of carbon elements in the MnS@C-1, MnS@C-2, and MnS@C-3 samples is 7.71, 24.42, and 34.04 wt.%, respectively.^[4a,9] The G-band in the Raman spectra of the samples (**Figure S10**, Supporting Information) is slightly blue-shifted with the increase of carbon content in the three samples, demonstrating the existence of a large amount of disordered but graphite-like carbon.

Field-emission scanning electron microscopy (FE-SEM) observation displays that MnS@C-1, MnS@C-2, and MnS@C-3 hollow nanospheres with different carbon shell thickness all retain the essential morphological features of the original nanospheres with a diameter of ca. 850 nm from the S@MnO₂ precursor without gross external changes, and the surface of nanospheres gradually becomes smoother and denser with increasing carbon coating content (**Figures 1e–g**). Moreover, the hollow structure was confirmed by SEM images of broken nanospheres. It can be estimated from the transmission electron microscopy (TEM) observation (**Figure S11**, Supporting Information) that the thickness of carbon coating layer in the MnS@C-1, MnS@C-2, and MnS@C-3 hollow nanospheres is ~5, 12.5, and 22.5 nm, respectively. The high angle annular dark-field scanning transmission electron microscopy (HAADF-STEM) and corresponding EDS mapping images of MnS@C-2 display that the outline of the hollow nanospheres for Mn element is well in accordance with S but slightly smaller than that of C element, attesting that the MnS shell is encapsulated by an outer carbon layer (**Figure 1h**). X-ray photoelectron spectroscopy (XPS) measurements were performed to analyze the chemical composition and element valence states of the hollow double-shell MnS@C-2 nanospheres (**Figure S12**, Supporting Information). The existence of Mn, S, C, N, and O elements was proved by the XPS survey. The peaks at 641.7 and 653.8 eV belong to Mn 2p_{3/2} and Mn 2p_{1/2} of Mn²⁺ in

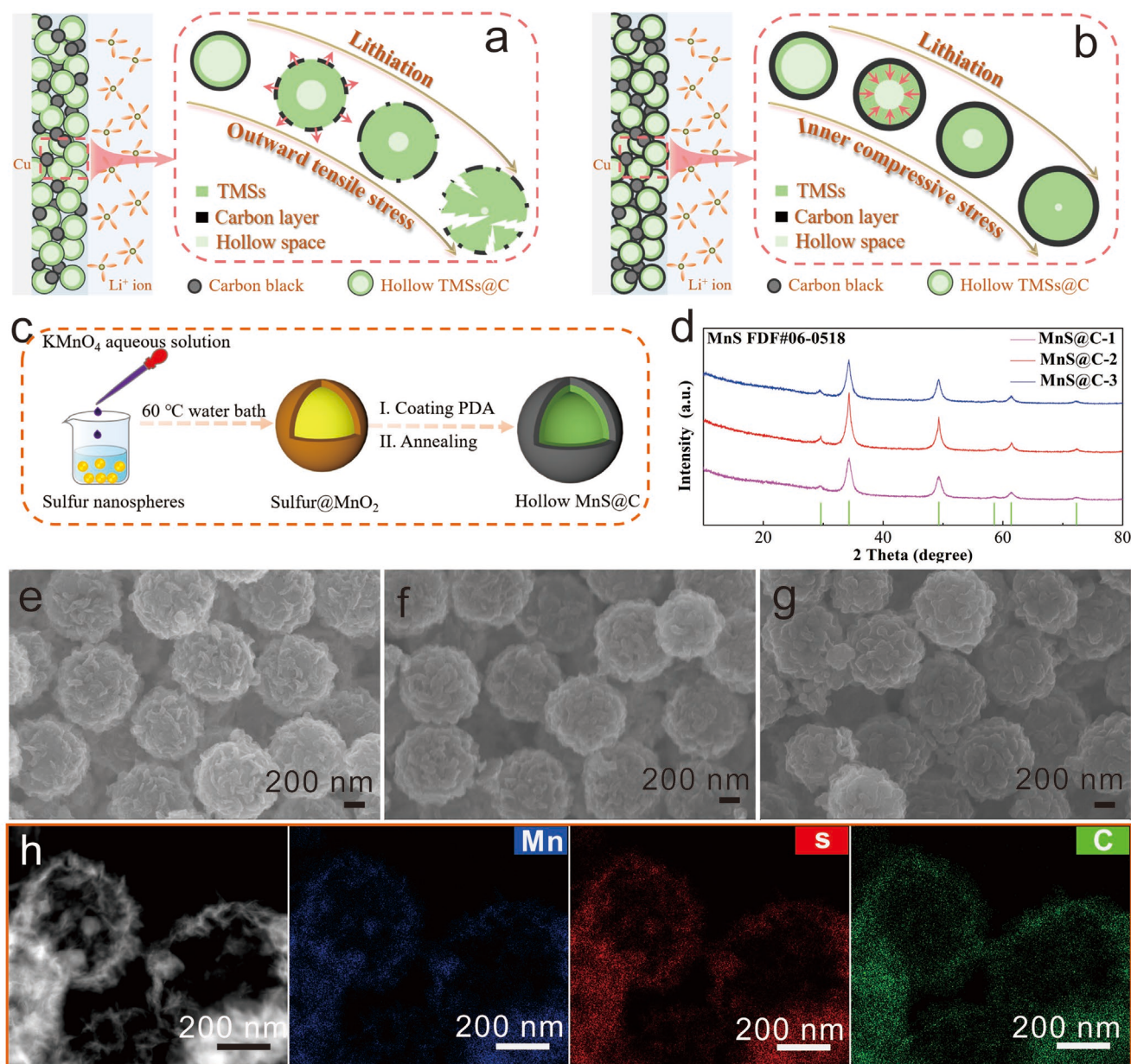


Figure 1. Expansion, synthesis, and characterization of hollow double-shell MnS@C nanospheres. a, b) Expansion schematic, c) formation process and d) XRD patterns. SEM images of e) MnS@C-1, f) MnS@C-2 and g) MnS@C-3 hollow nanospheres. h) HAADF-STEM image and the corresponding energy-dispersive X-ray spectroscopy (EDS) mapping for hollow MnS@C-2 nanospheres.

the Mn 2*p* spectrum, respectively. Besides, the fitting peak of Mn–S/C–S–Mn bonds can be clearly observed in the S 2*p* spectrum, further indicating the presence of MnS.^[4a,10]

2.2. Electrochemical Results of the Hollow Double-Shell MnS@C Structures

Li-ion half-cells were assembled to evaluate the electrochemical performance of hollow double-shell MnS@C nanospheres as an anode material using galvanostatic charge-discharge (GCD) and cyclic voltammetry (CV) techniques (Figure 2).

The MnS@C-2 electrode reveals an excellent initial discharge capacity of 858 mAh g⁻¹ at a larger current density of 2 A g⁻¹, and can retain 652 mAh g⁻¹ after 400 cycles, which is immensely higher than the corresponding results for the MnS@C-1 and MnS@C-3 electrodes (Figure 2a). Moreover, it can be clearly seen that the cycle stability of the MnS@C-2 and MnS@C-3 electrodes is almost the same, and obviously superior to that of the MnS@C-1 electrode. Meanwhile, TEM results (Figure S13, Supporting Information) after cycling indicate that the hollow structure in the MnS@C-1 electrode is broken and collapsed, while the hollow structure in the MnS@C-2 and MnS@C-3 electrodes does not change significantly, which can be ascribed

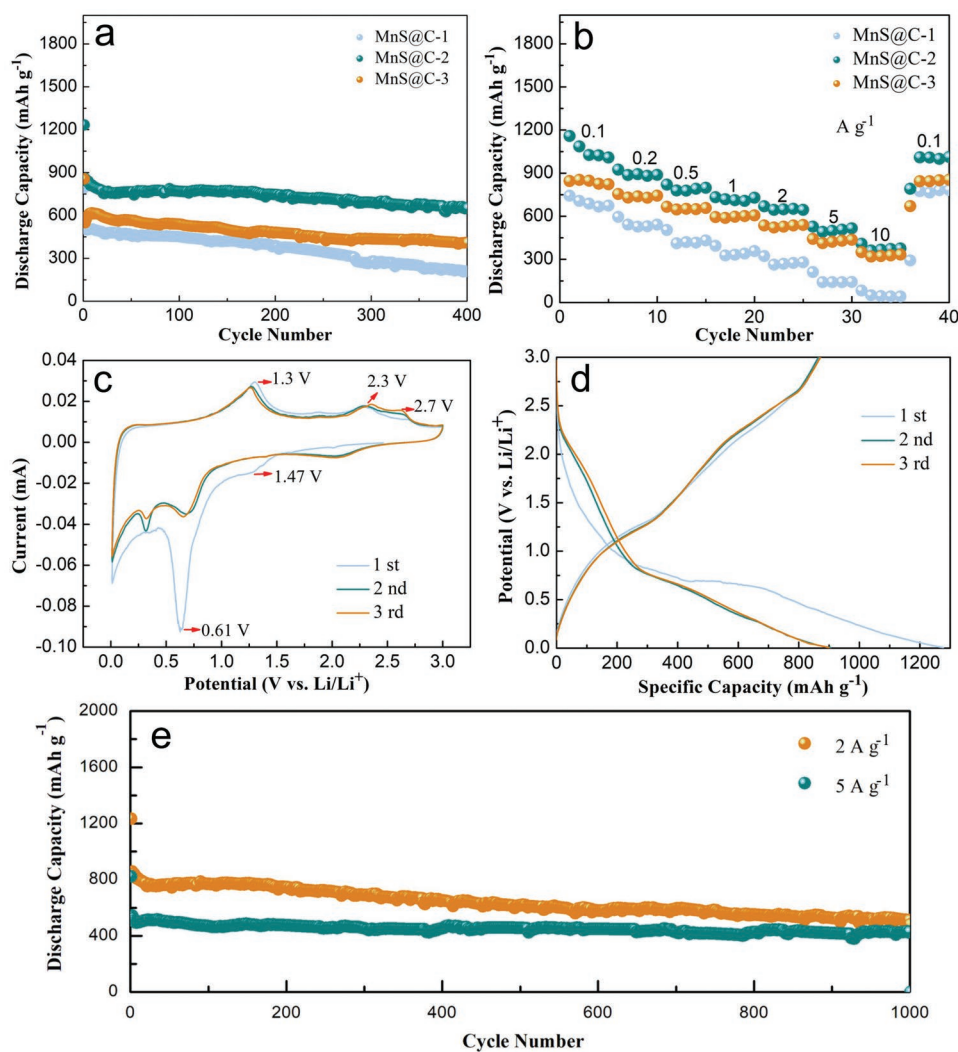


Figure 2. Electrochemical results for hollow double-shell MnS@C nanospheres. a) Cycling performances at 2 A g^{-1} . b) Rate performances. c) CV curves at a scan rate of 0.1 mV s^{-1} and d) discharge/charge voltage profiles of the MnS@C-2 electrode at 0.1 A g^{-1} . e) Long-cycling tests of the MnS@C-2 electrode at 2 and 5 A g^{-1} .

to the gradual nanoconfined behavior of the outer carbon shell on the expansion of the MnS during the process of lithiation when the thickness of carbon coating layers is increased and tailored. The reversible capacities of the MnS@C-2 electrode is decreased from 1157 to 886, 787, 711, 648, 498, and 366 mAh g^{-1} , with the increasing of current densities from 0.1 to 0.2, 0.5, 1, 2, 5, and 10 A g^{-1} , respectively (Figure 2b). When the current density is returned to 0.1 A g^{-1} , the specific capacity of the MnS@C-2 electrode comes back to 1024 mAh g^{-1} , displaying an excellent rate reversibility. However, the MnS@C-3 electrodes demonstrated capacities of 994, 755, 666, 594, 535, 441, and 350 mAh g^{-1} at 0.1, 0.2, 0.5, 1, and 2 A g^{-1} , respectively. When the current densities exceed 2 to 5 and 10 A g^{-1} for ultrafast charging/discharging, the MnS@C-3 electrode delivers comparable capacities with the MnS@C-2 electrode. In addition, the MnS@C-2 electrode has a smaller interface resistance value of 125Ω , which is much lower than that of the MnS@C-1 (350Ω) and MnS@C-3 (175Ω) electrodes (Figure S14, Supporting Information).

Typical CV curves were obtained in the potential range of 0.01 – 3.0 V versus Li^+/Li at 0.1 mV s^{-1} , which can confirm the electrochemical reaction processes during charging and discharging (Figure 2c). A unique CV curve of the first cathodic process different from the subsequent CV cycles can be observed, in which the poor anodic peak at ca. 1.47 V can be attributed to the formation of Li_2MnS_x phase due to the insertion of Li ions, with further decrease of the cell potential. The stronger reduction peak at ca. 0.61 V can be assigned to the solid electrolyte interphase (SEI) and the irreversible structure transition from $\alpha\text{-MnS}$ to $\beta\text{-MnS}$ phase.^[2b,11] In the subsequent cycles, three pairs of redox peaks appear in the CV curves, manifesting a three-step process during the electrochemical conversion reaction. From the anodic scan process of the second cycle, the oxidation peaks at ca. 1.3 and 2.3 V can be attributed to electrochemical reactions from the reduction products of Mn metal and Li_2S_x in the first cathodic process to the Li_2MnS_x intermediate, and finally generating MnS through lithium extraction, respectively.^[9b,12] In addition, the broad characteristic of the

anodic scan peak at 2.7 V should be due to the formation of MnS_{1+z} ($0 < z \leq 1$) from further oxidation of Mn^{2+} in MnS .^[13] In the opposite cathodic process, the electrochemical redox reactions are reversible, indicating excellent delithiation behaviors. Typical electrochemical characteristics with one clear plateau are also revealed in the charging/discharging curves of the MnS@C-2 electrodes (Figure 2d). These yielded a Coulombic efficiency of ca. 70% for the first charging/discharging curves, which is associated with SEI formation. From the second cycle, the Coulombic efficiency is close to 100% and the charging/discharging curves have a negligible shape change between the second and third cycles. Actually, MnS@C-2 electrodes showed an ultralong cyclic stability at large current densities of 2 and 5 A g^{-1} (Figure 2e). It can be seen that the specific capacity of the electrode gradually fades from 858 to 512 mAh g^{-1} at 2 A g^{-1} during 1000 cycles, and the average capacity decay is only 0.346 mAh g^{-1} per cycle. Apparently, the electrode exhibits a high capacity of 539 mAh g^{-1} with the increase of the current density to 5 A g^{-1} , and retains 430 mAh g^{-1} after 1000 cycles with a high-capacity retention ratio of 80%, indicating superior cycling performance. Furthermore, the MnS@C electrodes revealed a high discharge specific capacity of 553 mAh g^{-1} under a large loading mass of 4 mg cm^{-2} at a higher current density of 2 A g^{-1} and can be maintained at ca. 400 mAh g^{-1} after 200 cycles (Figure S15a, Supporting Information). Hence, it can be found that the rate performance and cyclic stability of the hollow MnS@C structures are better than those reported in previous literature (Figures S15b,c, Supporting Information). In addition, the assembled Li-ion full cells with commercial LiFePO_4 show an acceptable discharge specific capacity of ca. 70 mAh g^{-1} at 0.5 A g^{-1} after 60 cycles (Figures S16, Supporting Information).

2.3. Finite Element Analysis of Hollow Double-Shell MnS@C Structure During Lithiation

In order to fundamentally explore the stress management of outer carbon layers with different thicknesses on the lithiation expansion process of MnS , finite element analysis (FEA) was performed to simulate the interfacial stress between lithiated MnS and outer carbon layer (Figures 3a–c). It can be seen from the stress distributions of all hollow double-shell MnS@C nanospheres after full lithiation (Figures 3a-1,2,c-1,2) that the drastic volume expansion caused by lithiation generates a large outward tensile stress between MnS and the carbon layer with the thickness of ca. 5 nm in the hollow double-shell MnS@C-1 nanospheres, which indicates a failure restriction of MnS expansion to the internal hollow space, and this situation finally leads to structural failure (Figures 3a-1,2). The tensile stress of the inner MnS layer evolves into lower compressive stress with the increasing of carbon shell thickness to ca. 12.5 nm in the hollow double-shell MnS@C-2 nanospheres (Figures 3b-1,2). Moreover, the compressive stress in the MnS layer increases from the interface to the inner surface, resulting in the expansion of MnS on the inner surface into the central hollow space. When the carbon layer is supplied with a thickness of ca. 22.5 nm, the lower compressive stress of inner MnS layer is completely transformed into stronger compressive stress (Figures 3c-1,2).

Thus, the hollow double-shell MnS@C-3 structure with thicker carbon shell retained mechanical stability at the last stage of lithiation, and demonstrated an ability to constrain the drastic volume expansion of MnS . Subsequently, the stress value of MnS layer under different lithiation states was simulated for all hollow structures, in which negative and positive values in the vertical axis represent tensile stress and compressive stress, respectively. For the hollow double-shell MnS@C-1 nanospheres, the tensile stress extremely increases from the initial -9.52 to -6.91 GPa when lithiation reached 60%, and then slowly to -6.42 GPa in the 100% lithiation state, proving that the volume expansion of MnS layer is always from inside to outside during the whole lithiation process (Figures 3a-3). However, the compressive stress of MnS layer in the MnS@C-2 and MnS@C-3 hollow nanospheres both reveal a monotonically decreasing trend from the 0% to 100% lithiation state. Meanwhile, the MnS layer of MnS@C-3 nanospheres in fully lithiation states (100% lithiation) exhibits larger compressive stress of 10.3 GPa compared with MnS@C-2 (7.73 GPa) due to the thickness increase of outer carbon coating layer (Figures 3b-3,c-3), further showing the mechanical stability of hollow double-shell MnS@C structures with thicker carbon layers.

2.4. Multiple-Scale In Situ Characterization Analysis of Hollow Double-Shell MnS@C Structures

Morphology and structure evolution of hollow double-shell MnS@C structure were analyzed by in situ TEM during the process of lithiation expansion (Figures 4a,b). For the hollow MnS@C-1 nanospheres (Video S1, Supporting Information), the lithiation process starts when $\text{Li}_2\text{O/Li}$ probe contacted with working electrode (Figure S17a, Supporting Information), and after 720 s of lithiation, the diameter of hollow MnS@C nanosphere rapidly increases from an initial 837 to 970 nm (Figure S17b, Supporting Information). While in the next lithiation process also of 720 s duration, an increased diameter of only 29.2 nm can be observed for the hollow double-shell MnS@C nanosphere (Figure S17c, Supporting Information), indicating that the dramatic volume expansion occurred during the initial stage of lithiation due to outer larger tensile stress distribution, which is consistent with the FEA results. Compared with the hollow MnS@C-1 nanosphere, the diameter of the hollow MnS@C-2 nanosphere changes from 902 to 987 nm in the lithiation process of 0–1440 s (Figures 4c,e and Video S2, Supporting Information), showing the restriction of MnS volume expansion when a thicker outer carbon layer is in place. Moreover, the conversion reaction mechanism of lithium storage can be confirmed according to electron diffraction patterns (EDPs), in which the MnS is gradually converted into Mn metal and Li_2S throughout the progress of lithiation reactions (Figures 4d,f). The hollow double-shell MnS@C-3 nanosphere with carbon layer of 22.5 nm reveals a smaller diameter variation from 929 to 976 nm, demonstrating that the volume expansion of MnS is further effectively restrained by the increased carbon coating thickness (Figures S17d,f and Video S3, Supporting Information). Meanwhile, according to the diameter variation trends of all hollow double-shell MnS@C structures during the whole lithiation process (Figure 4g), it is clearly seen

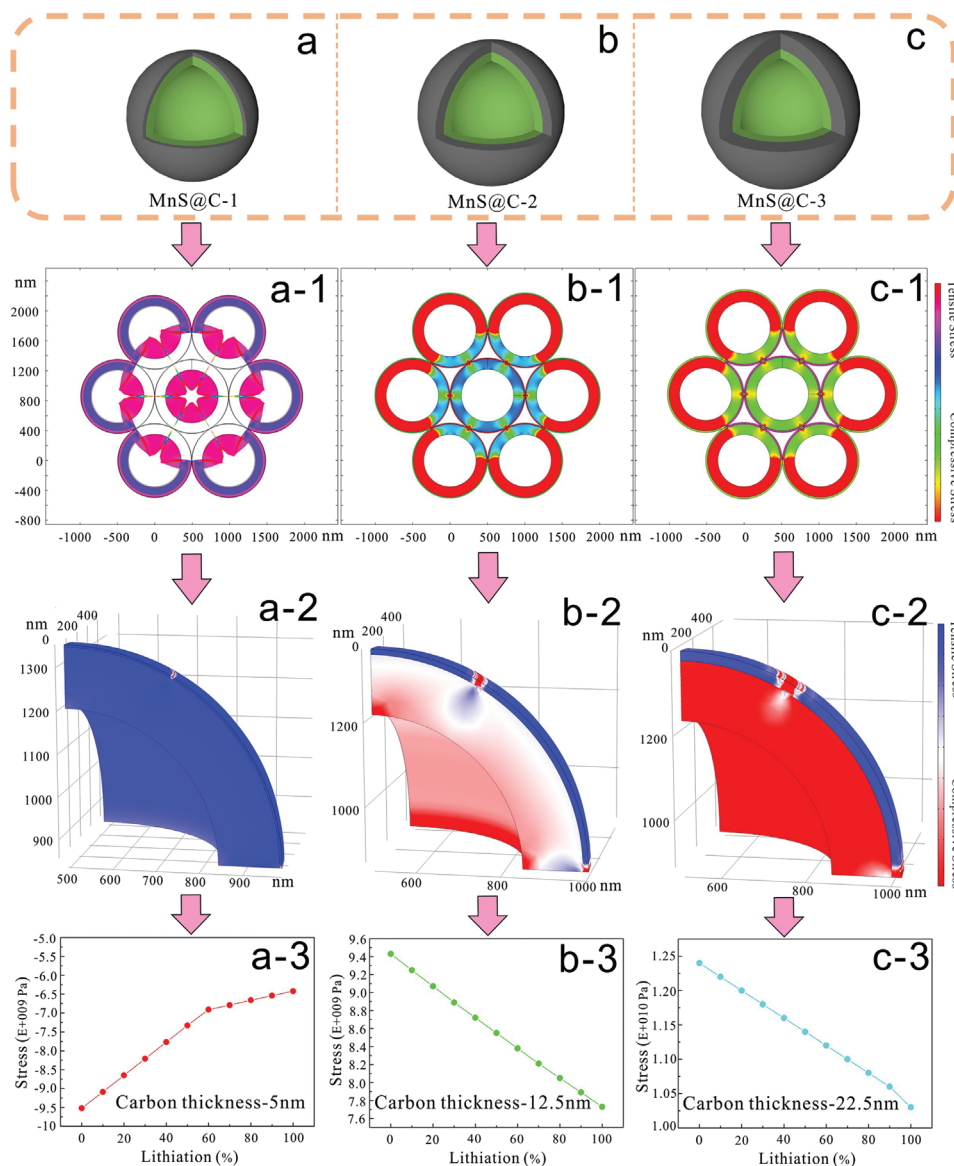


Figure 3. Finite element analysis of the hollow double-shell MnS@C nanospheres during lithiation. Schematic illustration of a) MnS@C-1, b) MnS@C-2 and c) MnS@C-3. Stress distribution of the a-1,2) MnS@C-1, b-1,2) MnS@C-2 and c-1,2) MnS@C-3 in their 100% lithiation state. Stress trends of the a-3) MnS@C-1, b-3) MnS@C-2 and c-3) MnS@C-3 in different lithiation states.

that the diameter increment of the MnS@C-1, MnS@C-2 and MnS@C-3 hollow nanospheres gradually decreases from the initial 162 to 85 nm, and finally to 47 nm with increasing thickness of the outer carbon layer, respectively. In addition, the corresponding calculated volume expansion rate indicates that the maximum volume expansion of 169% is displayed in the hollow double-shell MnS@C-1 nanospheres with their thin carbon layers, while the hollow MnS@C-3 nanospheres with thicker carbon layers exhibit the minimum volume expansion of 115%.

Subsequently, the expansion behavior of all hollow double-shell MnS@C nanospheres electrodes was further observed by the utilization of purpose-manufactured optical microscopic imaging system during discharging/charging (Figure 5a; Figure S18, Supporting Information). For the MnS@C-1 electrode (Figure S19 and Video S4, Supporting Information), the

thickness of electrodes during their first discharge gradually increased from the initial 37.4 to 82.4 μm with progressive lithiation states from 0 to 100%, while the electrode thickness of $\sim 33.5 \mu\text{m}$ was measured at the end of the first charging, which can be ascribed to the reforming of electrode structure due to the large volume expansion of the hollow MnS@C-1 nanospheres and the existence of interspaces between nanoparticles. In the second and third cycles, the thickness of MnS@C-1 electrodes in the delithiated state remained at 33.5 μm , revealing excellent electrode reversibility. Compared with the MnS@C-1 electrode, the MnS@C-2 electrode displays a decreased thickness variation from 91.3 to 124.5 μm because of the inhibiting effect of thicker carbon layer to MnS expansion behavior in hollow structure (Figures 5b, c; Figure S20 and Video S5, Supporting Information). With an increase of carbon coating

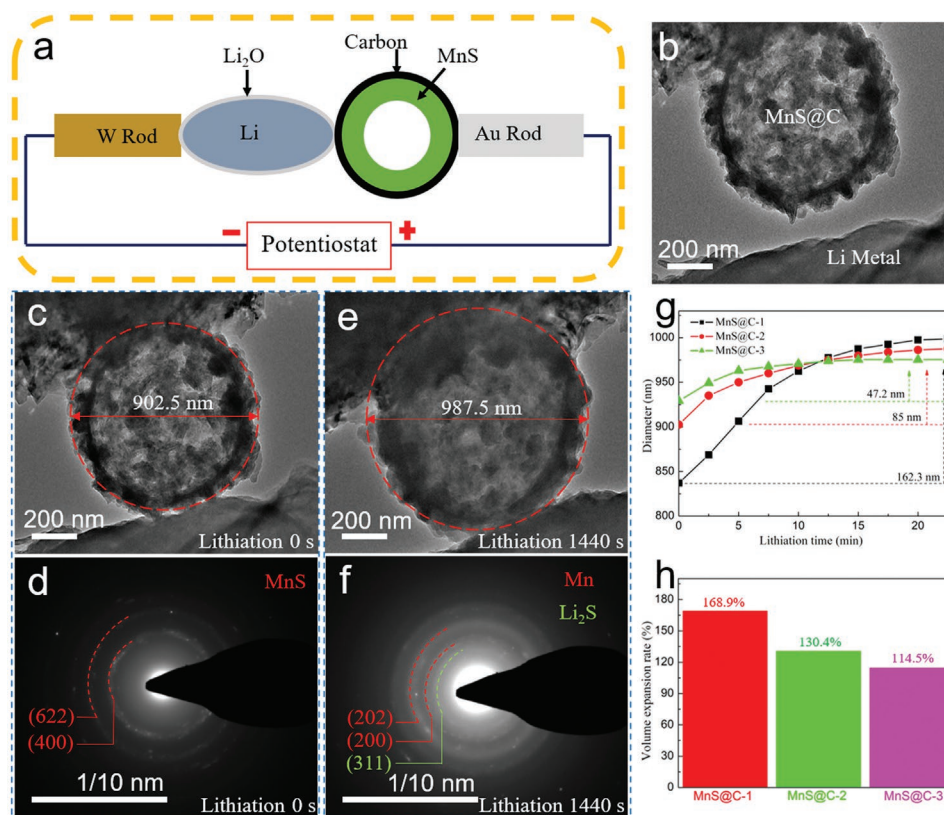


Figure 4. In situ TEM characterization of hollow double-shell MnS@C nanospheres. a) Schematic illustration of in situ TEM measurements. b) TEM image of MnS@C-2. c–f) TEM images and EDPs images of MnS@C-2 during lithiation. g) Diameter trends and h) volume expansion rates during lithiation.

layer, the thicker MnS@C-3 electrodes with initial thickness of 102 μm expanded to 138 μm after 100% lithiation (Figure S21 and Video S6, Supporting Information). Moreover, according to the thickness variation trends of all electrode types during the first three cycles of charging-discharging, it can be seen that the thickness change of MnS@C-1, MnS@C-2 and MnS@C-3 electrodes is 45, 33.2, and 36.1 μm , respectively (Figure 5d). Meanwhile, the calculated volume expansion rate of the MnS@C-2 electrode (136.3%) is similar to that of the MnS@C-3 electrode (135.3%), both lower than that of the MnS@C-1 electrode with the huge value of 220.3% (Figure 5e), which indicates that the controllable operation of shell thickness on the hollow structures can effectively alleviate the expansion of the electrode (Figure S22, Supporting Information).

3. Conclusion

In summary, a self-template approach was developed to produce hollow double-shell MnS@C nanospheres with long cycling stability for lithium storage anodes. The synthesis strategy is versatile and can be easily extended to prepare other carbon-coated TMSs hollow structures, such as $\text{Fe}_{1-x}\text{S}@C$ and $\text{SnS}@C$. Furthermore, the hollow MnS@C nanospheres reveal the outstanding improvement of cycling performance with the optimization of interfacial stress. Owing to a large outward tensile stress between core and shell during lithiation, MnS

cores exhibit a drastic volume expansion when the carbon shell from the hollow structure is ca. 5 nm, which finally leads to structural failure and poor cyclic stability. When the thickness of carbon layer is adjusted to ca.12.5 nm, the internal hollow space can accommodate the huge volume expansion of the MnS core with the transformation from tensile stress to compressive stress, indicating an excellent nano-confinement effect of the hollow structure, conferring long-cyclic performance. We believe that this work not only presents a general synthesis strategy for metal sulfide anodes with hollow nanostructures but also provides a new research platform from nano to macroscales and understanding of the volume expansion behavior of high-capacity electrode materials during energy storage.

4. Experimental Section

Synthesis of Sulfur Nanospheres Template: All the chemicals were purchased and used without further purification. Sulfur nanospheres template was obtained by a slight modification of the previous method.^[8] HCl solution (8 mL, 10 M) was slowly added dropwise to 1000 mL of aqueous solution consisting of polyvinylpyrrolidone surfactant (PVP, 0.2 g) and sodium thiosulfate ($\text{Na}_2\text{S}_2\text{O}_3 \cdot 5\text{H}_2\text{O}$, 9.925 g) and then stirred for 2 h at room temperature. After that, the suspension was filtered and washed with deionized water and dried overnight to obtain the sulfur nanospheres template.

Synthesis of S@MnO₂ Core-Shell Nanospheres: The as-prepared sulfur nanospheres template material (800 mg) was ultrasonically redispersed in 500 mL of PVP aqueous solution for 2 h, and then KMnO_4 solution

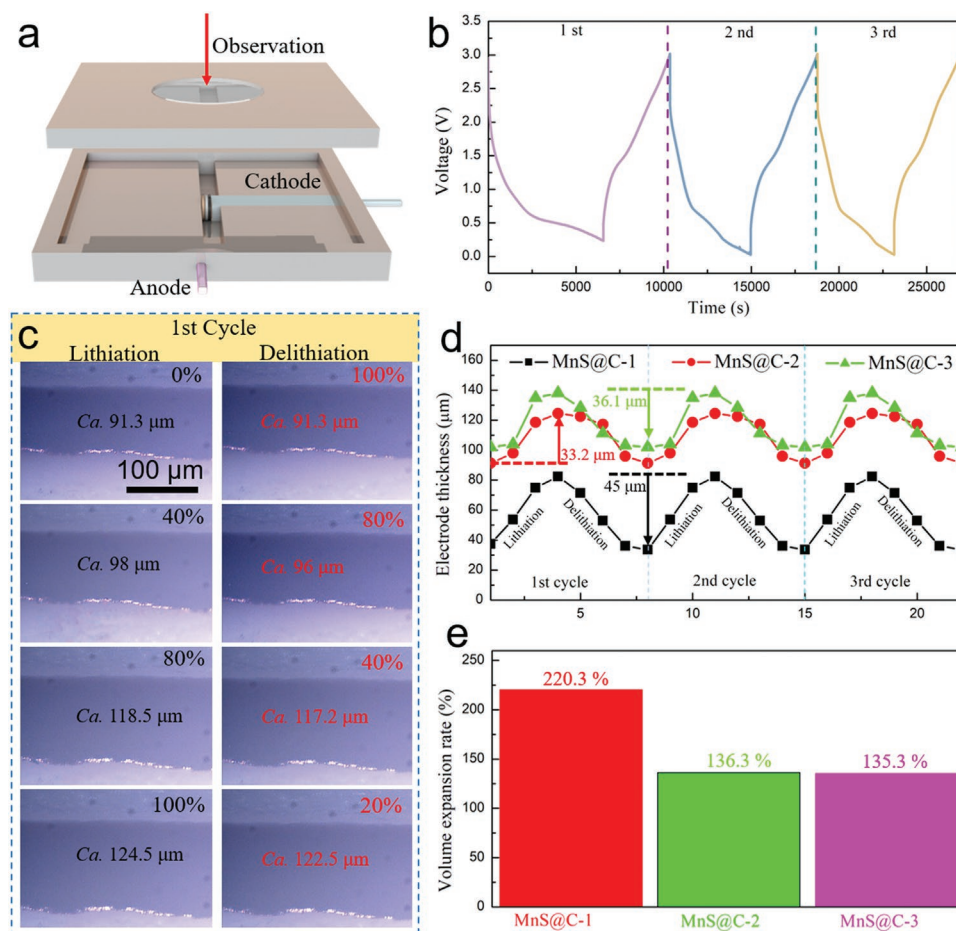


Figure 5. In situ optical observations of the hollow double-shell MnS@C nanospheres electrodes. a) Schematic illustration of in situ optical observations. b) discharge/charge voltage profiles and optical images of the MnS@C-2 electrode at 0.3 A g^{-1} . c) Optical images of the MnS@C-2 electrode during 1st cycle. d) Thickness trends and e) volume expansion rates.

(0.028 M, 100 mL) was added to the above solution and stirred for 2 h at 60°C to form a black-brown precipitate. Finally, the precipitate was filtered and washed with deionized water to prepare the S@MnO₂ core-shell nanospheres.

Synthesis of Hollow Double-Shell MnS@C Nanospheres: First, 60 mg of tris hydrochloride ($\text{C}_4\text{H}_{11}\text{NO}_3\cdot\text{HCl}$) was added to 100 mL aqueous solution of the S@MnO₂ precursor (150 mg) under ultrasound. Second, the S@MnO₂@polydopamine precursor was obtained by adding 20 mg of dopamine monomer into the above solution after stirring for 20 h, filtering, and drying. Finally, the hollow double-shell MnS@C nanospheres (MnS@C-1) were prepared via heat treatment at 500°C for 2 h under argon atmosphere. For comparison, the MnS@C-2 and MnS@C-3 hollow nanospheres with different carbon content were synthesized by adding 30 mg and 40 mg of dopamine monomer respectively into the S@MnO₂ precursor solution, without changing other conditions.

Synthesis of Hollow Double-Shell Fe_{1-x}S@C Nanospheres: The synthetic route followed the above work with slight modifications. A mixed solution of $\text{FeCl}_3\cdot 6\text{H}_2\text{O}$ (252.9 mg) and urea (200 mg) was dropped into an aqueous solution containing S nanospheres templates (150 mg) and PVP surfactant (60 mg). Subsequently, the mixed solution was transferred into a high-pressure reaction kettle and heated at 80°C for 12 h to obtain orange S@FeOOH precursor. 60 mg of $\text{C}_4\text{H}_{11}\text{NO}_3\cdot\text{HCl}$ was further added to 100 mL aqueous solution of the S@FeOOH precursor (100 mg) under ultrasound, and then the S@FeOOH@polydopamine precursor was obtained by adding 70 mg of dopamine monomer into

the above solution after stirring for 20 h, filtering and freeze-drying. Finally, the hollow double-shell Fe_{1-x}S@C nanospheres were prepared via heat-treatment at 500°C for 2 h under argon atmosphere.

Synthesis of Hollow Double-Shell SnS@C Nanospheres: The synthetic route is similar to that of the hollow Fe_{1-x}S@C nanospheres. Typically, 2.5 mL of $\text{SnCl}_4\cdot 5\text{H}_2\text{O}$ (530 mg) hydrochloric acid solution and 600 mg of urea were sequentially added to 100 mL of S nanospheres template solution. Then the above solution was transferred into a high-pressure reaction kettle and heated at 80°C for 8 h to obtain white S@SnO(OH)₂ precursor. 60 mg of tris-hydrochloride was further added to 100 mL aqueous solution of the S@SnO(OH)₂ precursor (100 mg) under ultrasound, and the S@FeOOH@polydopamine precursor was further obtained by adding 60 mg of dopamine monomer into the above solution after stirring for 20 hours, filtering and freeze-drying. Finally, the hollow double-shell SnS@C nanospheres was prepared via heat-treatment at 500°C for 2 h under argon atmosphere.

All of these preparation processes can be extended to a scalable scale at the gram level.

Material Characterization: The crystalline structure of the as-prepared samples was tested using XRD, (Rigaku Smart Lab, Japan). The morphology, microstructure and particle size distribution were characterized by FE-SEM, (Carl Zeiss Super55 operated at 5 kV), TEM, (Hitachi HT7700 operated at 120 kV) equipped with EDS and laser particle sizer (Malvern nano 90). XPS was performed to examine the surface chemical states of the samples using a Kratos XSAM-800 spectrometer with monochromatized Al K α radiation. The Raman

spectra was carried out on a Horiba (LabRam HR-800) spectrometer (532 nm, 50 mW excitation laser) in the range of 500 – 2200 cm⁻¹. The carbon content of the samples was measured by TGA under air with a heating rate of 5 °C min⁻¹.

Electrochemical Characterization: Electrochemical behaviors were carried out in 2032 type coin cells with pure lithium foil as both counter and reference electrode. Working electrodes were prepared by coating a slurry composed of the MnS@C active materials, binder (poly(vinylidene fluoride)) and conductive agent (acetylene black) at a weight ratio of 8:1:1 on Cu foil and dried in a vacuum oven at 80 °C for 12 h. The batteries were assembled in an Ar-filled glovebox using Celgard 2400 separators and 1 M LiPF₆ in a 1:1:1 of ethylene carbonate, diethyl carbonate, and dimethyl carbonate as electrolyte. GCD measurements were performed on a LAND CT2001 multichannel battery testing system within a voltage window of 0.01 – 3.0 V, and the discharge specific capacity can be calculated based on the total mass of electroactive MnS and carbon coating layer in the hollow double-shell MnS@C structures. In addition, the activation process of half cells was performed at a lower current density of 0.1 A g⁻¹ before the cyclic performance measurements. CV and electrochemical impedance spectroscopy tests were carried out on a CHI 660E electrochemical workstation at a scanning rate of 0.1 mV s⁻¹ within a voltage range of 0.01 – 3.0 V.

In Situ TEM Observations: The expansion behavior of the hollow double-shell MnS@C nanospheres during lithiation was observed on a FEI Talos 20 at 200 kV using a TEM-STM holder (PicoFemto, FE02-ST). The MnS@C hollow nanospheres were placed on an Au tip and then connected to a W tip coated by the Li/Li₂O, in which the natural Li₂O on the surface of lithium metal served as the solid-state electrolyte. Lithiation was controlled by applying a negative voltage bias.

In Situ Optical Observations: In-situ observations were carried out in optical cells with quartz windows (LIB-MS-1, Beijing Scistar Technology Co., Ltd), in which the MnS@C cathode disk, separator, and Li foil anode in close contact are perpendicular to the quartz window. A metallographic microscope (LW750LJT China) with a fitted charge-coupled device camera was applied to monitor the expansion behavior of the MnS@C electrodes.

Finite Element Analysis: The simulation was based on the thermal expansion stress model, which was derived from an abstract simplification of the experiment, and integrated modeling and meshing functions were used to calculate and process the results through COMSOL Multiphysics 5.6. The MnS and C layers were simulated to be isotropic and linearly elastic, and the coefficient of thermal expansion was assumed constant, in which the diameter of the cavity and the thickness of the MnS layer in the hollow double-shell MnS@C structures were set to 700 nm and 135 nm, respectively, as well as three values of the carbon coating thickness with 5 nm, 12.5 nm and 22.5 nm. The ring section representing MnS and C material was combined by a point connection mode, and the outer-periphery of the carbon layer was set as the fixed load boundary condition. The degree of lithiation was simulated by calculating the different sizes of circumferential expansion. The corresponding parameters are in the supporting information (Table S1).

Supporting Information

Supporting Information is available from the Wiley Online Library or from the author.

Acknowledgements

Z.M. and A.S. contributed equally to this work. This work was financially supported by the National Natural Science Foundation of China (52074241, 52174281, 51674221, and 51704261), the Natural Science Foundation of Hebei Province (B2021203016 and B2018203360), the Science and Technology Project of Hebei Education Department

(BJ2020038) and Cultivation Project for Basic Research and Innovation of Yanshan University (2021LGDZ013). Z.M., A.S., Y.F., X.Q., G.S. thank the support of the Subsidy for Hebei Key Laboratory of Applied Chemistry after Operation Performance (22567616H). H.T. acknowledges support from the Faculty of Science Seed Funding from University of Technology Sydney.

Open access publishing facilitated by University of Technology Sydney, as part of the Wiley - University of Technology Sydney agreement via the Council of Australian University Librarians.

Conflict of Interest

The authors declare no conflict of interest.

Data Availability Statement

The data that support the findings of this study are available in the supplementary material of this article.

Keywords

anode materials, cyclic stability, hollow structures, lithium-ion batteries, manganese sulfide, volume expansion

Received: January 31, 2023

Revised: February 27, 2023

Published online: March 28, 2023

- [1] a) P. Albertus, S. Babinec, S. Litzelman, A. Newman, *Nat. Energy* **2018**, *3*, 16; b) G. Harper, R. Sommerville, E. Kendrick, L. Driscoll, P. Slater, R. Stolkin, A. Walton, P. Christensen, O. Heidrich, S. Lambert, A. Abbott, K. S. Ryder, L. Gaines, P. Anderson, *Nature* **2019**, *575*, 75; c) Y. M. Sun, N. A. Liu, Y. Cui, *Nat. Energy* **2016**, *1*, 16071; d) J. Liu, Z. N. Bao, Y. Cui, E. J. Dufek, J. B. Goodenough, P. Khalifah, Q. Y. Li, B. Y. Liaw, P. Liu, A. Manthiram, Y. S. Meng, V. R. Subramanian, M. F. Toney, V. V. Viswanathan, M. S. Whittingham, J. Xiao, W. Xu, J. H. Yang, X. Q. Yang, J. G. Zhang, *Nat. Energy* **2019**, *4*, 180; e) H. Tian, H. Tian, S. Wang, S. Chen, F. Zhang, L. Song, H. Liu, J. Liu, G. Wang, *Nat. Commun.* **2020**, *11*, 5025; f) H. Tian, J. Liang, J. Liu, *Adv. Mater.* **2019**, *31*, 1903886.
- [2] a) P. B. Geng, S. S. Zheng, H. Tang, R. M. Zhu, L. Zhang, S. Cao, H. G. Xue, H. Pang, *Adv. Energy Mater.* **2018**, *8*, 1703259; b) D. H. Liu, W. H. Li, Y. P. Zheng, Z. Cui, X. Yan, D. S. Liu, J. W. Wang, Y. Zhang, H. Y. Lu, F. Y. Bai, J. Z. Guo, X. L. Wu, *Adv. Mater.* **2018**, *30*, 1706317; c) X. J. Wei, Y. B. Zhang, B. K. Zhang, Z. Lin, X. P. Wang, P. Hu, S. L. Li, X. Tan, X. Y. Cai, W. Yang, L. Q. Mai, *Nano Energy* **2019**, *64*, 103899; d) Y. L. Zhou, J. Tian, H. Y. Xu, J. Yang, Y. T. Qian, *Energy Storage Mater.* **2017**, *6*, 149; e) T. Y. Hou, B. R. Liu, X. H. Sun, A. R. Fan, Z. K. Xu, S. Cai, C. M. Zheng, G. H. Yu, A. Tricoli, *ACS Nano* **2021**, *15*, 6735; f) Q. D. Li, L. Li, P. J. Wu, N. Xu, L. Wang, M. Li, A. Dai, K. Amine, L. Q. Mai, J. Lu, *Adv. Energy Mater.* **2019**, *9*, 1901153.
- [3] a) J. Wang, X. Guo, X. Du, J. Liang, J. Wu, G. Zhao, X. Li, S. Gui, F. Zheng, J. Zhao, C. Xu, D. Wang, H. Yang, B. Zhang, Y. Zhu, *Energy Storage Mater.* **2022**, *51*, 11; b) X. Ou, L. Cao, X. Liang, F. Zheng, H. S. Zheng, X. Yang, J. H. Wang, C. Yang, M. Liu, *ACS Nano* **2019**, *13*, 3666; c) K. Chen, G. Li, Z. Hu, Y. Wang, D. Lan, S. Cui, Z. Li, A. Zhao, Y. Feng, B. Chen, W. Chen, L. Mi, Y. Huang, *Chem. Eng. J.* **2022**, *435*, 135149.

- [4] a) X. J. Xu, S. M. Ji, M. Z. Gu, J. Liu, *ACS Appl. Mater. Int.* **2015**, *7*, 20957; b) Y. Feng, Y. L. Zhang, Y. Z. Wei, X. Y. Song, Y. B. Fub, V. S. Battaglia, *Phys. Chem. Chem. Phys.* **2016**, *18*, 30630; c) C. J. He, Y. Q. Wang, W. J. Meng, J. Zhang, Y. Xie, Y. L. Hou, D. L. Zhao, *J. Alloys Compd.* **2021**, *889*, 161648; d) M. L. Chen, Z. Y. Zhang, L. P. Si, R. B. Wang, J. J. Cai, *ACS Appl. Mater. Interfaces* **2019**, *11*, 35050; e) Z. Jiao, P. D. Zhao, Y. C. He, L. Ling, W. F. Sun, L. L. Cheng, *J. Alloys Compd.* **2019**, *809*, 151854; f) R. A. P. Camacho, A. M. Wu, X. Z. Jin, X. F. Dong, X. N. Li, H. Huang, *J. Power Sources* **2019**, *437*, 226931; g) Z. Syum, B. Venugopal, A. Sabbah, T. Billo, T. C. Chou, H. L. Wu, L. C. Chen, K. H. Chen, *J. Power Sources* **2021**, *482*, 228923; h) X. Z. Jin, H. Huang, A. M. Wu, S. Gao, M. K. Lei, J. J. Zhao, X. X. Gao, G. Z. Cao, *ACS Nano* **2018**, *12*, 8037; i) G. Li, K. Chen, Y. Wang, Z. Wang, X. Chen, S. Cui, Z. Wu, C. Soutis, W. Chen, L. Mi, *Nanoscale* **2020**, *12*, 8493.
- [5] a) R. Tan, J. L. Yang, J. T. Hu, K. Wang, Y. Zhao, F. Pan, *Chem. Commun.* **2016**, *52*, 986; b) W. W. Sun, X. C. Tao, P. P. Du, Y. Wang, *Chem. Eng. J.* **2019**, *366*, 622; c) Z. L. Chen, R. B. Wu, H. Wang, Y. K. Jiang, L. Jin, Y. H. Guo, Y. Song, F. Fang, D. L. Sun, *Chem. Eng. J.* **2017**, *326*, 680; d) Y. M. Chen, X. Y. Li, K. Park, L. M. Zhou, H. T. Huang, Y. W. Mai, J. B. Goodenough, *Angew. Chem., Int. Ed.* **2016**, *55*, 15831; e) W. W. Chen, T. T. Li, Q. Hu, C. P. Li, H. Guo, *J. Power Sources* **2015**, *286*, 159; f) Z. Cui, S. A. He, J. Q. Zhu, M. L. Gao, H. Wang, H. Zhang, R. J. Zou, *Small Methods* **2022**, *6*, 2101484; g) S. Y. Wan, X. Liu, L. K. Fu, C. B. Zhou, H. Y. Chen, G. H. Li, S. Y. Cao, Q. M. Liu, *J. Alloys Compd.* **2021**, *870*, 159407; h) H. Tian, F. Huang, Y. Zhu, S. Liu, Y. Han, M. Jaroniec, Q. Yang, H. Liu, G. Q. M. Lu, J. Liu, *Adv. Funct. Mater.* **2018**, *28*, 1801737; i) H. Tian, H. Tian, W. Yang, F. Zhang, W. Yang, Q. Zhang, Y. Wang, J. Liu, S. R. P. Silva, H. Liu, G. Wang, *Adv. Funct. Mater.* **2021**, *31*, 2101796; j) H. Tian, X. Liu, L. Dong, X. Ren, H. Liu, C. A. H. Price, Y. Li, G. Wang, Q. Yang, J. Liu, *Adv. Sci.* **2019**, *6*, 1900807.
- [6] a) J. Y. Wang, Y. Cui, D. Wang, *Adv. Mater.* **2019**, *31*, 1801993; b) L. Yu, H. B. Wu, X. W. Lou, *Acc. Chem. Res.* **2017**, *50*, 293; c) Y. Xiao, J. Y. Hwang, I. Belharouak, Y. K. Sun, *Nano Energy* **2017**, *32*, 320.
- [7] a) B. Li, J. Wang, R. Bi, N. Yang, J. Wan, H. Jiang, L. Gu, J. Du, A. Cao, W. Gao, D. Wang, *Adv. Mater.* **2022**, *34*, 2200206; b) S. Gao, N. Wang, S. Li, D. Li, Z. Cui, G. Yue, J. Liu, X. Zhao, L. Jiang, Y. Zhao, *Angew. Chem., Int. Ed.* **2020**, *59*, 2465.
- [8] Q. Li, Z. P. Ma, J. J. Li, Z. Liu, L. K. Fan, X. J. Qin, G. J. Shao, *ACS Appl. Mater. Interfaces* **2020**, *12*, 35049.
- [9] a) S. Utsumi, J. Miyawaki, H. Tanaka, Y. Hattori, T. Itoi, N. Ichikuni, H. Kanoh, M. Yudasaka, S. Iijima, K. Kaneko, *J. Phys. Chem. B* **2005**, *109*, 14319; b) K. M. Jeon, J. S. Cho, Y. C. Kang, *J. Power Sources* **2015**, *295*, 9.
- [10] a) J. B. Goodenough, Y. Kim, *Chem. Mater.* **2010**, *22*, 587; b) H. Tian, A. L. Song, P. Zhang, K. A. Sun, J. J. Wang, B. Sun, Q. H. Fan, G. J. Shao, C. Chen, H. Liu, Y. D. Li, G. X. Wang, *Adv. Mater.* **2023**, *35*, 2210714.
- [11] T. F. Zhou, W. K. Pang, C. F. Zhang, J. P. Yang, Z. X. Chen, H. K. Liu, Z. P. Guo, *ACS Nano* **2014**, *8*, 8323.
- [12] D. H. Ha, T. Ly, J. M. Caron, H. T. Zhang, K. E. Fritz, R. D. Robinson, *ACS Appl. Mater. Interfaces* **2015**, *7*, 25053.
- [13] a) Y. Ma, Y. J. Ma, G. T. Kim, T. Diemant, R. J. Behm, D. Geiger, U. Kaiser, A. Varzi, S. Passerini, *Adv. Energy Mater.* **2019**, *9*, 1901153; b) B. L. Liu, Z. J. Liu, D. Li, P. Q. Guo, D. Q. Liu, X. N. Shang, M. Z. Lv, D. Y. He, *Appl. Surf. Sci.* **2017**, *416*, 858.